Light scattering by multiple red blood cells

He, Jiangping; Karlsson, Anders; Swartling, Johannes; Andersson-Engels, Stefan

Published in:
Journal of the Optical Society of America A: Optics and Image Science, and Vision

DOI:
10.1364/JOSAA.21.001953

2004

Light scattering by multiple red blood cells

Jiangping He and Anders Karlsson

Department of Electroscience, Lund University, Box 118, 221 00 Lund, Sweden

Johannes Swartling and Stefan Andersson-Engels

Department of Physics, Lund University, Box 118, 221 00 Lund, Sweden

Received August 20, 2003; revised manuscript received February 19, 2004; accepted May 27, 2004

The interaction of light with multiple red blood cells was systematically investigated by the finite-difference time-domain method (FDTD). The simulations showed that the lateral multiple scattering between red blood cells is very weak and that the polarization has an almost insignificant influence on the distribution of the scattered light. The numerical results of the FDTD method were compared with the results from the Rytov approximation and the discrete dipole approximation (DDA). The agreement with the DDA was excellent.

OCIS codes: 170.0170, 290.0290.

1. INTRODUCTION

Today laser light is a common tool for medical examination and treatment. Consequently there is a medical interest in the light-scattering properties of tissue. It has an influence in dosimetry of laser therapy,[1–3] light-scattering spectroscopy for tissue diagnostic purposes,[4–6] and optical analysis of blood for blood-related diseases.[7,8] For all these applications the optical properties of the blood play an important role. These applications motivate efforts in improving experiments, theory, and numerical simulations in blood optics. In this paper the scattering from multiple blood cells is numerically analyzed by a full-wave method as well as by approximate methods.

It is known that the scattering and absorption of light in blood are largely governed by the red blood cells (RBCs). It is their refractive index, as well as their size, shape, and orientation, that determines how light propagates. A previous paper[9] presents an investigation of the interaction of light with a single RBC. It was shown that approximate methods that utilize that the RBC is a weakly scattering object provided accurate results. In experiments the blood can be diluted so that the blood cells are sparsely distributed. In that case approximate multiple-scattering methods based on the Monte Carlo method are applicable.[10] The parameters used in these methods can be determined from a single-blood-cell calculation. In whole blood the concentration of RBCs may be as high as 50%, and the multiple-scattering effects have to be considered. In a recent paper[11] the boundary-element method was applied to the scattering from multiple blood cells. In that case the blood cells were aggregated in an axially symmetric rolleau, and this symmetry was utilized to reduce the problem to two dimensions. Otherwise there seem to be very few reports on scattering from multiple blood cells.

The aim of this paper is twofold. One objective is to investigate the limitations of the finite-difference time-domain (FDTD) method, the Rytov approximation, and the discrete dipole approximation (DDA) for the case of multiple blood cells within a small volume. In the numerical examples there are up to six blood cells in the modeled region. The other objective is to analyze the scattered intensities from multiple RBCs. That includes the analysis of cross polarization, the dependence on the orientation of the RBCs, and the dependence of the refractive index. The shapes of the RBCs are realistic (i.e., discocyte-like shape) in all of the calculations.

In Section 2 the geometry, the material parameters, the incident field, and the scattered fields are defined. Section 3 contains short descriptions of the FDTD method, the Rytov approximation, and the DDA method. The numerical results are collected in Section 4, and in Section 5 some concluding remarks are given.

2. PRELIMINARIES

The refractive index for the RBC is denoted as n_1, and the refractive index of the surrounding blood plasma is denoted as n_2. For the wavelengths assumed in this paper, the absorption is very low, and for this reason it is neglected in both regions, even though the numerical methods are capable of including it. The model of the disklike normal RBC used in the simulations is defined in Refs. 12 and 13 with an RBC volume of 94 μm^3. Figure 1 shows the cross section of the disklike RBC model, where the enclosing box has height $a = 2.547\,\mu$m and length $b = 7.76\,\mu$m. The three-dimensional (3D) shape is obtained by rotating the cross section around the z axis. Figure 2 depicts the 3D picture of the disklike RBC model. The membrane of RBCs has a negligible influence on the scattered field (see Refs. 14 and 15), and hence the RBC model does not include the membrane or any other internal structure. In the simulations the incident wave is a time-harmonic linearly polarized plane wave that propagates in the positive z direction. The di-

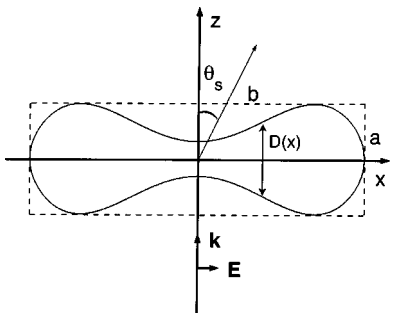

Fig. 1. RBC cross section, where $D(x) = [1 - (x/R_0)^2]^{1/2}[C_0 + C_2(x/R_0)^2 + C_4(x/R_0)^4]$ and $R_0 = 3.91\,\mu$m, $C_0 = 0.81\,\mu$m, $C_2 = 7.83\,\mu$m, and $C_4 = -4.39\,\mu$m, which corresponds to a volume of 94 μm^3.

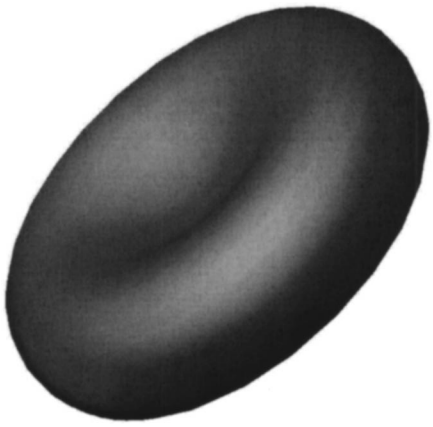

Fig. 2. 3D RBC.

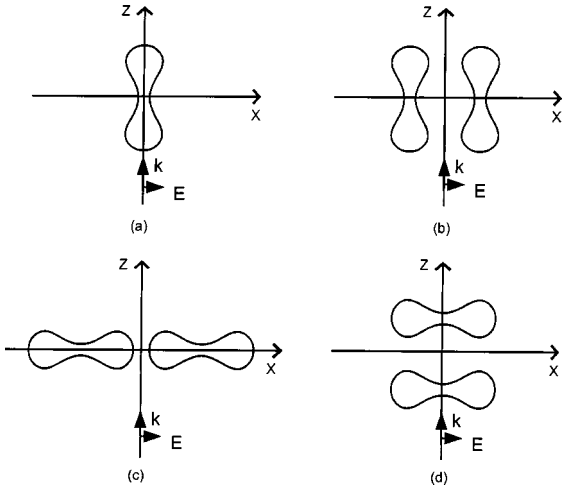

Fig. 3. Different geometries used in the simulations.

rection of the electric field is along the vector $\hat{\xi}$, which is a vector in the xy plane. With the time convention $\exp(-i\omega t)$, the complex incident electric field is given by

$$\mathbf{E}_{\text{inc}}(z) = \hat{\xi} E_0 \exp(ikz), \tag{1}$$

where $k = n_2\omega/c_0$ is the wave number for the plasma and c_0 is the velocity of light in vacuum. In the numerical examples the RBCs are oriented so that their axis of symmetry is parallel either to the z axis or to the x axis (see Fig. 3). To interrelate the angular distributions of the scattered light of different incident angles, we calculate the scattering probability as a function of the zenith scattering angle θ_s (see Fig. 1). The scattering probability $P(\theta_s)$ is defined as the integral of the differential scattering cross section $\sigma_{\text{diff}}(\theta_s, \phi)$ over all azimuthal angles $\phi \in [0, 2\pi]$:

$$P(\theta_s) = \frac{\int_0^{2\pi} \sigma_{\text{diff}}(\theta_s, \phi)\sin\theta_s \, \mathrm{d}\phi}{\int_0^{2\pi}\int_0^{\pi} \sigma_{\text{diff}}(\theta, \phi)\sin\theta \, \mathrm{d}\theta\mathrm{d}\phi}. \tag{2}$$

The differential cross section is defined by

$$\sigma_{\text{diff}}(\theta, \phi) = r^2 \frac{\langle \mathbf{S}_s(r, \theta, \phi) \cdot \hat{r}\rangle}{\langle \mathbf{S}_{\text{inc}} \cdot \hat{z}\rangle}, \tag{3}$$

where

$$\langle \mathbf{S}_s(r, \theta, \phi)\rangle = \frac{1}{2}\mathrm{Re}[\mathbf{E}(r, \theta, \phi) \times \mathbf{H}^*(r, \theta, \phi)] \tag{4}$$

$$\langle \mathbf{S}_{\text{inc}}\rangle = \frac{1}{2}\mathrm{Re}[\mathbf{E}_{\text{inc}}(z) \times \mathbf{H}^*_{\text{inc}}(z)]$$

$$= \frac{1}{2}\frac{n_2}{\eta_0}|E_0|^2\hat{z} \tag{5}$$

are the time averages of the Poynting vector of the scattered and incident fields, respectively. Furthermore, $\hat{r}$ is the radial unit vector, $\mathbf{E}(r, \theta, \phi)$ is the scattered electric field, $\mathbf{H}^*(r, \theta, \phi)$ is the complex conjugate of the corresponding magnetic field, and $\eta_0 = 120\pi\,\Omega$ is the wave impedance of vacuum. Note that $P(\theta_s)\mathrm{d}\theta$ is the probability that a photon is scattered in the angular interval $(\theta_s, \theta_s + \mathrm{d}\theta)$.

The far-field amplitude $\mathbf{F}(\theta, \phi)$ of the scattered field is defined by

$$\lim_{r\to\infty}\mathbf{E}(r, \theta, \phi) = \mathbf{F}(\theta, \phi)\frac{\exp(ikr)}{kr}. \tag{6}$$

3. METHODS

In this section the methods that are applied to the RBC problem are described briefly.

A. Finite-Difference Time-Domain Method

The FDTD approach is general and flexible and was recently applied to biological scattering problems.[9,16–20] It permits the simulation of scattering from inhomogeneous objects of arbitrary shape. Today it is one of the best full-wave methods for accurate simulations of the scattering of light from a small number of blood cells. Readers interested in the FDTD method are recommended the book by Taflove.[21] The FDTD algorithm numerically solves Maxwell's curl equations in the time domain. To calculate the angular far-field distribution of the scattered light, we require several techniques.

Absorbing boundary condition. Because of the finite computational domain, the values of the fields on the boundaries must be defined so that the solution region ap-

pears to extend infinitely in all directions. With no truncation conditions the scattered waves are artificially reflected at the boundaries, leading to inaccurate results. In this paper split-type perfectly matched layers have been implemented in the 3D FDTD program. Each component of the electromagnetic field is split into two parts. In Cartesian coordinates the six components yield 12 subcomponents denoted as E_{xy}, E_{xz}, E_{yx}, E_{yz}, E_{zx}, E_{zy}, H_{xy}, H_{xz}, H_{yx}, H_{yz}, H_{zx}, and H_{zy}. The Maxwell equations are replaced by 12 equations. In our simulations eight perfectly matched layers are used. That gives a reflection coefficient of less than 10^{-8}. References 21 and 22 contain more detailed descriptions of perfectly matched lasers.

Total field/scattered field. The total field/scattered field formulation permits the introduction of the incident field in an elegant way (see Ref. 21). The computational grid is divided into two regions. The total field region encloses the scatterers, whereas the scattered field region, where only the scattered field components are stored, encloses the total field region, as illustrated in Fig. 4. At the border between the two regions, special connecting conditions are required, where the incident field is either added or subtracted from the total field.

Far-field transformation. The FDTD method is inherently a near-field method. To determine the far-field scattering pattern, we transform the near-field data to far-field data by the near-field-to-far-field transformation. The transformation used in this paper is from a surface integral representation of the scattered field. A comprehensive discussion of the near-field-to-far-field technique is found in Ref. 21.

B. Discrete Dipole Approximation

The DDA is closely related to the method of moments.[23] The principle of the method is as follows: The scattering volume is divided into N parts. Each part is small enough to be represented by a dipole moment. Linearity of the medium implies that the induced dipole moment is equal to the electric field in the volume multiplied by the polarizability of the volume. The evaluated electric field is calculated as a superposition of the field from the sources external to the object and the electric field from the sources inside the object, in this case the induced dipoles. The field from the external sources is the incident plane wave, and hence the electric field in volume j is given by

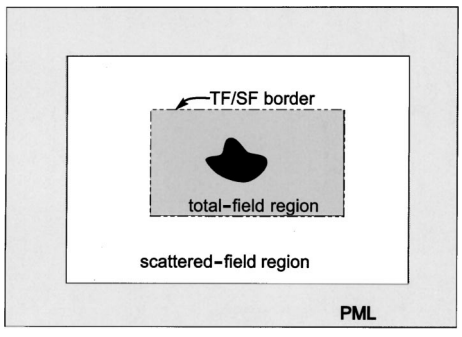

Fig. 4. Regions used by the FDTD method.

$$\mathbf{E}(\mathbf{r}_j) = \mathbf{E}_{\text{inc}}(\mathbf{r}_j) - \sum_{k \neq j} \mathbf{A}(\mathbf{r}_j, \mathbf{r}_k) \cdot \mathbf{p}(\mathbf{r}_k). \tag{7}$$

The term $-\mathbf{A}(\mathbf{r}_j, \mathbf{r}_k) \cdot \mathbf{p}(\mathbf{r}_k)$ is the electric field at position $\mathbf{r}_j$ from a dipole $\mathbf{p}(\mathbf{r}_k)$ at position $\mathbf{r}_k$ and can be found in basic textbooks in electromagnetic theory (see Ref. 24). The equation is usually not solved by direct inversion. Instead, iterative methods, e.g., the conjugate gradient method, are applied. A more detailed description of the DDA method is given in Refs. 23 and 25.

C. Superposition

The superposition approximation is based on the assumption that multiple-scattering effects are small between the cells. Each RBC is viewed as a scattering object, and the multiple-scattering effects between the RBCs are neglected. The advantage is the reduction of the CPU time and the required RAM of the computer. The far-field pattern is calculated by the FDTD method for each RBC, and then the far fields are added. In our RBC simulation models, the scattering objects are identical and have the same orientation. The far fields of the RBCs are the same, except for the phase shift. Thus it is enough to perform a simulation for one RBC and add a phase shift to get the total far field of the RBCs. Given the far-field amplitude $\mathbf{F}(\theta, \phi)$ [see Eq. (6)] of one RBC with the origin located at the center of the RBC, the far-field amplitude expression for the configuration of N RBCs reads as

$$\mathbf{F}_{\text{RBC}}(\theta, \phi) = \mathbf{F}(\theta, \phi) \sum_{n=1}^{N} \exp(ik\hat{r} \cdot \mathbf{d}_n), \tag{8}$$

where $\hat{r} = (\sin\theta\cos\phi, \sin\theta\sin\phi, \cos\theta)$, $\mathbf{d}_n$ is the translated vector of RBC n relative to the origin, and k is the wave number for the plasma. In the numerical examples it is shown that the method provides accurate results as long as the blood cells are located in directions lateral to the z axis.

D. Rytov Approximation

The Rytov approximation is a frequently used method in tomography (see Refs. 26 and 27), where it is utilized for the inverse-scattering problem of determining the internal structure of an object. In this paper it is applied in its simplest form to the scattering of a plane wave from objects in a homogeneous lossless medium. The method can be explained as follows: Consider an object that occupies the volume V. Let the index of refraction be n_1 for the object and n_2 for the surrounding medium. The incident wave is given by Eq. (1). The approximation assumes that when the wave passes the object, the phase of the wave is shifted while its amplitude and polarization are unaltered. The wave is assumed to travel along straight rays parallel to the z axis. If $z = z_1$ is a plane behind the object, the total electric field in that plane reads as

$$\mathbf{E}(x, y, z_1) = \hat{x}E_0 \exp\{ik_0[n_2 z_1 + (n_1 - n_2)d(x, y)]\}, \tag{9}$$

where $k_0 = \omega/c_0$ is the wave number in vacuum and $d(x, y)$ is the total distance that the ray travels inside the scattering object. Thus the phase is shifted an angle

$k_0(n_1 - n_2)d(x, y)$ compared with the incident wave. The far-field amplitude is given by the near-field to far-field transformation (see Ref. 21), i.e.,

$$\mathbf{F}(\theta, \phi) = i\frac{k^2}{4\pi}E_0 \exp(ikz_1)\hat{r} \times \int\int_S (\hat{y} - \hat{r} \times \hat{x}) \times \{\exp[ik_0(n_1 - n_2)d(x, y)] - 1\} \times \exp(-ik\hat{r} \cdot \mathbf{r})\mathrm{d}x\mathrm{d}y, \quad (10)$$

where S is the plane $z = z_1$. Note that the integrand is zero outside the projection of the blood cells on the plane $z = z_1$. All reflections of the wave are neglected. Consequently, the method is limited to scattering angles $\theta_s < \pi/2$. Despite these approximations the calculated far-field pattern is quite accurate for the single-RBC case. The advantages of the Rytov approximation are that it can easily be implemented on a computer and that it is a fast method.

4. RESULTS AND DISCUSSION

In this section the scattering properties of the RBCs are investigated by the FDTD method, the superposition approximation, the Rytov approximation, and the DDA method. The simulation program SEMCAD (Ref. 28) was used for the FDTD simulations of the far-field scattering pattern. In all of the simulation cases, the incident wavelength is 632.8 nm. The grid space was adaptively set between $\lambda/10$ and $\lambda/20$ in order to yield accurate results. The errors in the far-field amplitude are with this grid space everywhere less than 1%. This is confirmed by comparisons with Mie scattering and with the DDA method. Since the relative index of refraction n_2/n_1 is close to one, it is the wavelength and not the geometry that determines the required grid space. The examples indicate the maximum size of a sample that an FDTD program can handle with a modern personal computer. The largest sample in the examples contains six RBCs. That requires roughly 2 Gbytes of RAM and 10 h of CPU time. The simulations in this paper indicate that the Rytov approximation is somewhat faster than the DDA method. Both are considerably faster than the FDTD method. In the numerical examples there is no difference in accuracy between the DDA and FDTD approaches. The Rytov approximation and the superposition method neglect multiple scattering, and they provide accurate results only when the RBCs are located in directions lateral to the z axis (see Figs. 8–13 below).

In the numerical examples the indices of refraction of the RBC and of the plasma are $n_1 = 1.406$ and $n_2 = 1.345$, respectively (see Ref. 29), except in Subsection 4.D, where the influence of the index of refraction is investigated. The FDTD method is used in most of the numerical examples, but one could just as well have used the DDA, since it gives the same results. In a number of the graphs, the θ interval is restricted to angles less than 20°, since the scattering probability is very close to zero for larger angles.

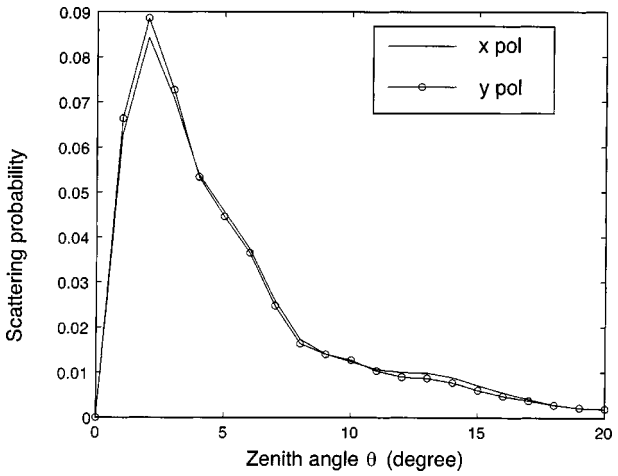

Fig. 5. Scattering probabilities of the RBC in Fig. 3(a) for polarization along the $\hat{x}$ and $\hat{y}$ directions.

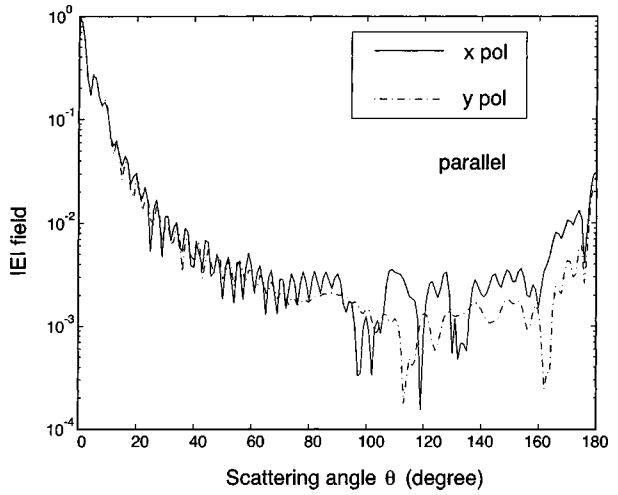

Fig. 6. Absolute value of the far-field amplitude of the electric field for the RBC in Fig. 3(a). Solid curve, far field in the xz plane for the incident field polarized in the x direction; dotted–dashed curve, far field in the yz plane for an incident field polarized in the y direction.

A. Influence of the Polarization

It is anticipated that cross polarization can appear in blood samples where the cells are aligned, e.g., in flowing blood, where the RBCs tend to align in a direction perpendicular to the flow direction. The question is whether the polarization effect is strong enough to be measurable. The far fields were calculated with the model presented in Fig. 3(a) for two orthogonal polarizations, one with $\hat{\xi} = \hat{x}$, i.e., with the electric field in the $\hat{x}$ direction, and the other with $\hat{\xi} = \hat{y}$ [see Eq. (1)]. The scattering probability patterns are shown in Fig. 5. Since the scattering probability [see Eq. (2)] is an averaged value over the azimuthal angle ϕ, the polarization effect almost disappears. This conclusion is in agreement with T-matrix results.[30] Figure 6 shows the absolute value of the electric far-field amplitude in the xz and yz planes in the cases of polarization in the $\hat{x}$ and $\hat{y}$ directions, respectively. The corresponding graphs for cross polarization are shown in Fig. 7. As seen from the graph, the effect that the polarization has on the far field is marginal. There will be a

small cross polarization if all RBCs are aligned as in Fig. 3(a). The simulations indicate that very accurate measurements are required in order to detect the cross polarization with samples containing few RBCs.

B. Scattering Probability for Models (b)–(d)

To investigate the dependence of the distance between two RBCs, we conducted systematic simulations by accurate FDTD calculations, as well as by superposition and by the Rytov approximation. Three cases were simulated. For each case the scattering probabilities were calculated for different distances between two RBCs [i.e., $0a$, $1a$, $2a$, and $3a$, where a is the thickness of the RBC (see Fig. 1)].

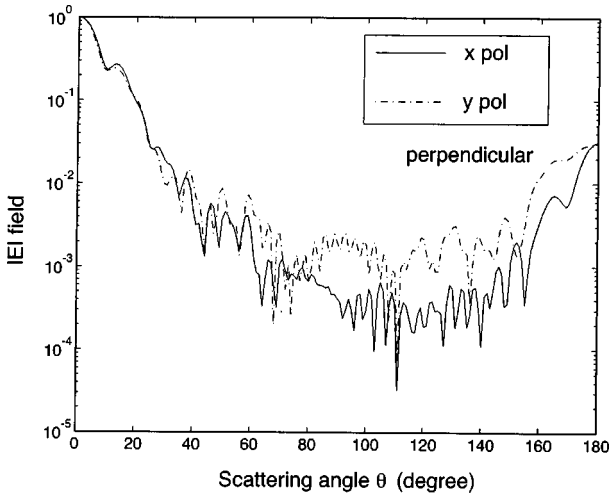

Fig. 7. Absolute value of the far-field amplitude of the electric field for the RBC in Fig. 3(a). Solid curve, far field in the yz plane for the incident field polarized in the x direction; dotted–dashed curve, the far field in the xz plane for an incident field polarized in the y direction.

1. Model (b) Case

Figure 8 shows the influence that the distance between cells has on the scattering probability. The scattering pattern becomes more complex when the RBC distance increases. Interestingly, the superposition method provides accurate results, even when the two RBCs touch. These results emphasize that the lateral multiple scattering is very weak between RBCs.

2. Model (c) Case

The same simulations as those in the previous case were conducted for the geometry in Fig. 3(c). The results are presented in Fig. 9. The scattering patterns are almost independent of the lateral distance. The superposition method is accurate because of the weak lateral multiple scattering between RBCs. Also, the Rytov approximation provides similar results (not shown).

3. Model (d) Case

The scattering patterns for the geometry in Fig. 3(d) are similar to those of model (c) (see Fig. 10). The superposition method does not work as well as in models (b) and (c). This means that the multiple scattering along the incident wave direction is more pronounced than in the lateral case and cannot be neglected. The Rytov approximation results of model (d) support this conclusion (see Fig. 11). Since the simplest form of the Rytov approximation is used, there is no difference between simulation results for different distances in model (d) [see Eq. (9)]. The DDA method was also applied to model (d). Figure 12

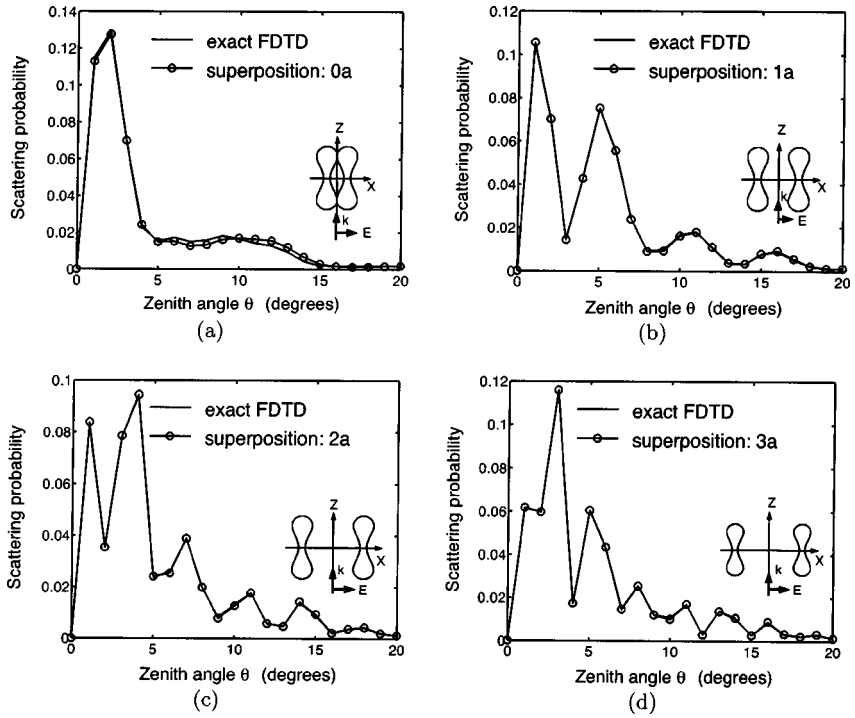

Fig. 8. Scattering probability for the geometry in Fig. 3(b) with four different separation distances. Plots (a), (b), (c), and (d) are the results with separation distances equal to $0a$, $1a$, $2a$, and $3a$, respectively, where a is the thickness of the RBC cross section (see Fig. 1).

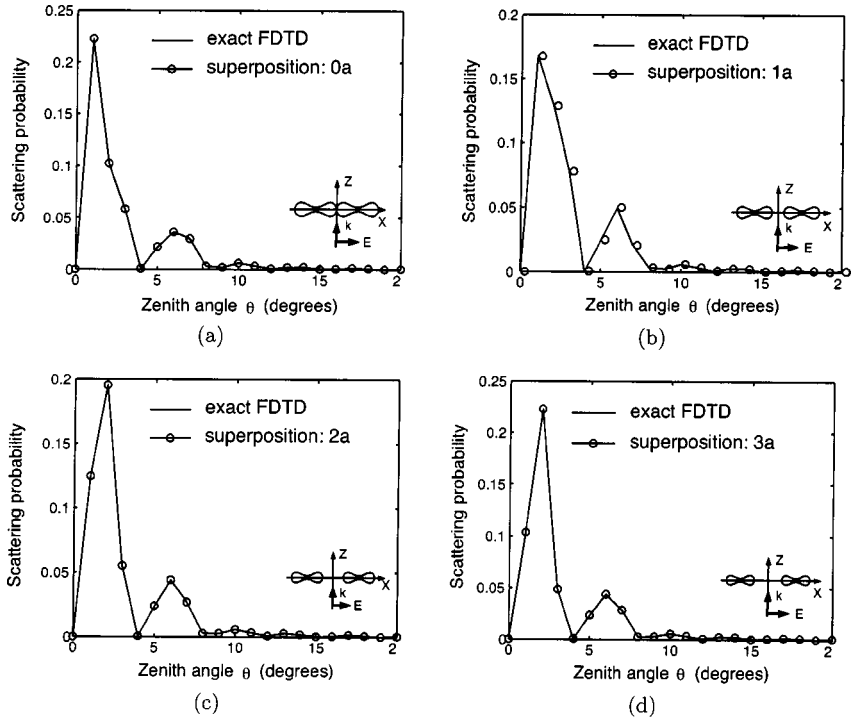

Fig. 9. Same case as that in Fig. 8 but for model (c). The superposition method, where the far fields for two single RBCs are added, gives virtually the same results as those from an FDTD calculation of the entire region. The multiple scattering is negligible.

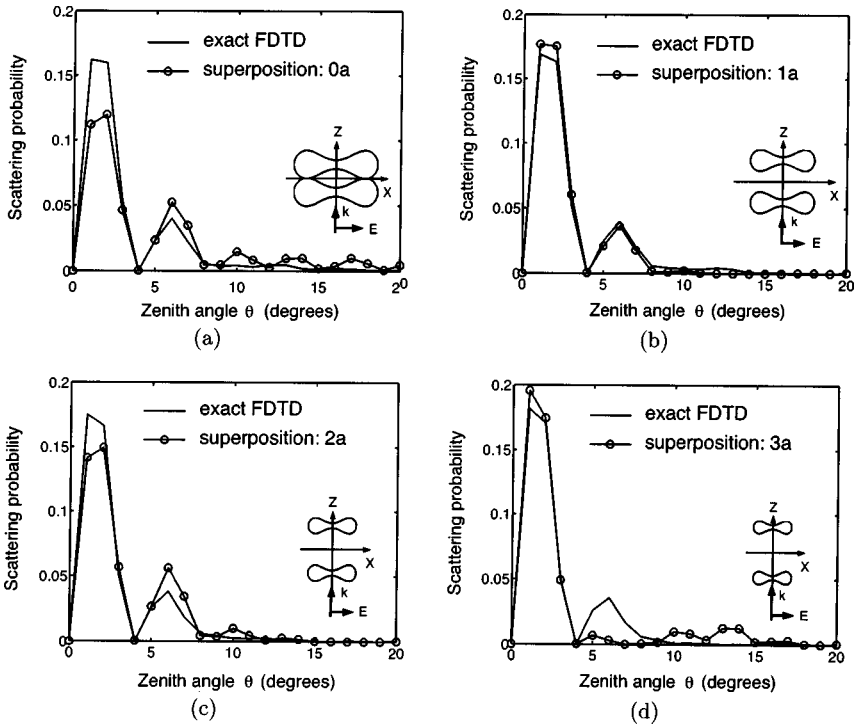

Fig. 10. Same case as that in Fig. 8 but for model (d). The superposition method, where the far fields for two single RBCs are added, does not give the same result as that from an FDTD calculation of the entire region. The multiple scattering is not negligible.

shows the result when the RBC distance equals $0a$ for model (d). It is seen that the DDA method can deal with the multiple scattering. As mentioned above, the DDA method provides the same accuracy as that of the FDTD method for all of the examples in this paper.

C. Scattering Probability for Multiple Red Blood Cells

In Subsection 4.B it was seen that the superposition method provides accurate results as long as the blood cells are located in directions lateral to the direction of propagation of the incident wave. Figure 13 shows the

scattering patterns of multiple RBCs. The simulation geometry is the same as that in Fig. 3(b), except that the number of RBCs is changed. Our simulation results show that one may calculate the scattering probability for many parallel RBCs by dividing the large simulation domain into small and computable subdomains along directions perpendicular to the incident wave direction.

D. Dependence of Refractive Index

To investigate the dependence of the refractive index, we altered the refractive index of the plasma, n_2, while keeping the refractive index of the RBC fixed at $n_1 = 1.406$. This corresponds to a situation where a liquid that changes the index of refraction of the plasma is added to the blood. Three different indices of refraction were used in this case (i.e., $n_2 = n_1/1.020$, $n_1/1.010$, $n_1/1.007$). It is interesting that the normalized scattering patterns of these three cases are almost the same. An approximate estimation of the scattered power from an RBC with relative index of refraction $n_r = n_1/n_2$ close to unity can be obtained by the Born approximation.[31] According to the Born approximation, the scattered field of an object with n_r close to unity is

$$\mathbf{E}_s(r,\ \theta,\ \phi) = -\frac{k^2 \exp(ikr)}{4\pi r}\hat{k}_s \times (\hat{k}_s \times \hat{e}_i)(n_r^2 - 1) \times \int\int\int_{\mathrm{RBC}} \mathrm{d}x'\,\mathrm{d}y'\,\mathrm{d}z' \times \exp[i(\mathbf{k}_i - \mathbf{k}_s) \cdot \mathbf{r}']. \tag{11}$$

Here k is the wave number of the plasma, $\mathbf{k}_i$ is the wave vector of the incident field, $\mathbf{k}_s$ is the wave vector of the scattered field, $\hat{k}_s = \mathbf{k}_s/k$, and $\mathbf{r} = (x', y', z')$. To see the variation in the scattered far field when the index of refraction of the plasma is changed, we analyzed the ratio of the scattered far fields for two different backgrounds. The ratio reads as

$$\frac{\mathbf{E}'}{\mathbf{E}} \sim \left(\frac{k'}{k}\right)^2 \frac{n_r'^2 - 1}{n_r^2 - 1}[1 + O(\delta k)], \tag{12}$$

where k and k' are the wave numbers in the two backgrounds and $\delta k = k' - k$. The corresponding ratio of the radiated powers reads as

$$\frac{P'}{P} \sim \left(\frac{1 - n_r^2}{1 - n_r'^2}\right)^2. \tag{13}$$

In Table 1 the radiated powers for different background refractive indices are listed. The results from relation (13) with $n_r' = 1.007$ and $P' = 4.33 \times 10^{-15}$ are also given in the table. The FDTD simulation results and that of the Born approximation have the same order of magnitude. The accuracy of the Born approximation improves as the relative refractive index approaches one.

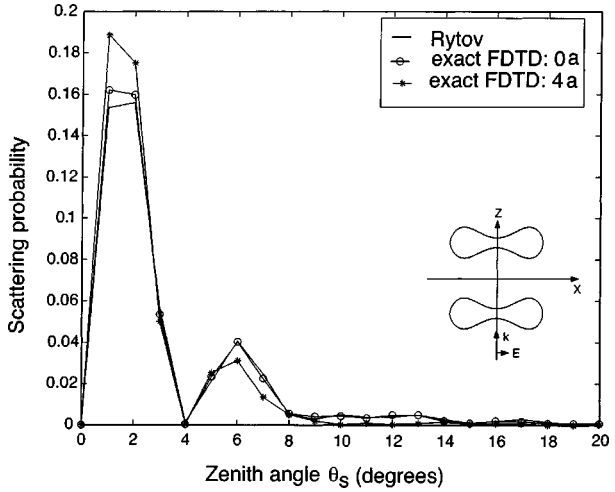

Fig. 11. Scattering probability obtained by the FDTD method and the Rytov approximation for the geometry in Fig. 3(d) with distances $0a$ and $4a$ between the RBCs.

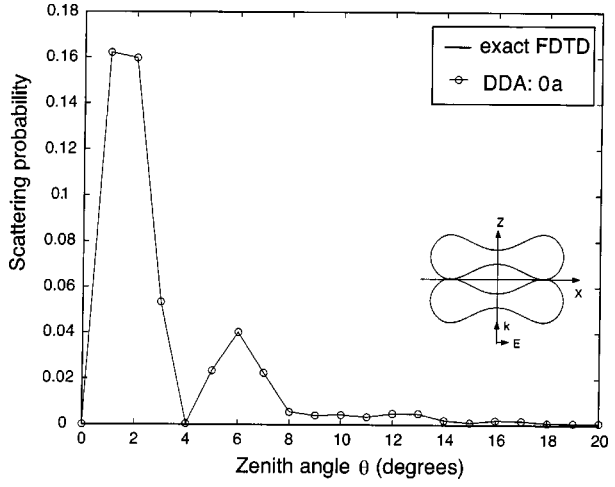

Fig. 12. Scattering probability obtained from the FDTD method and the DDA simulations for the geometry in Fig. 3(d) with distance $0a$ between the RBCs.

5. CONCLUSIONS

The scattering from several RBCs is analyzed. Two methods, FDTD and DDA, give identical and accurate results. Since the DDA method is related to the method of moments (see Ref. 24), it is expected that the method of moments is also a suitable method for blood optics. The boundary-element method, which is based on a surface integral equation, is also related to the method of moments. The boundary-element method has successfully been applied to blood optics (see Refs. 11 and 32). The Rytov approximation and the superposition method are limited to configurations where the multiple-scattering effects are small. From the simulation results it is seen that there is a weak polarization dependence in the far-field pattern from a single RBC. This is in agreement with the published results of T-matrix calculations.[30] It implies that there are cross-polarization effects when polarized light propagates through a sample of blood if the blood cells are aligned. The effect is weak, in particular in the forward direction, and it might not be possible to detect the cross polarization in an experiment. The scattering probability patterns are not sensitive to the polarization because of the integration in the azimuthal angle. The general and flexible numerical approach of the FDTD method was

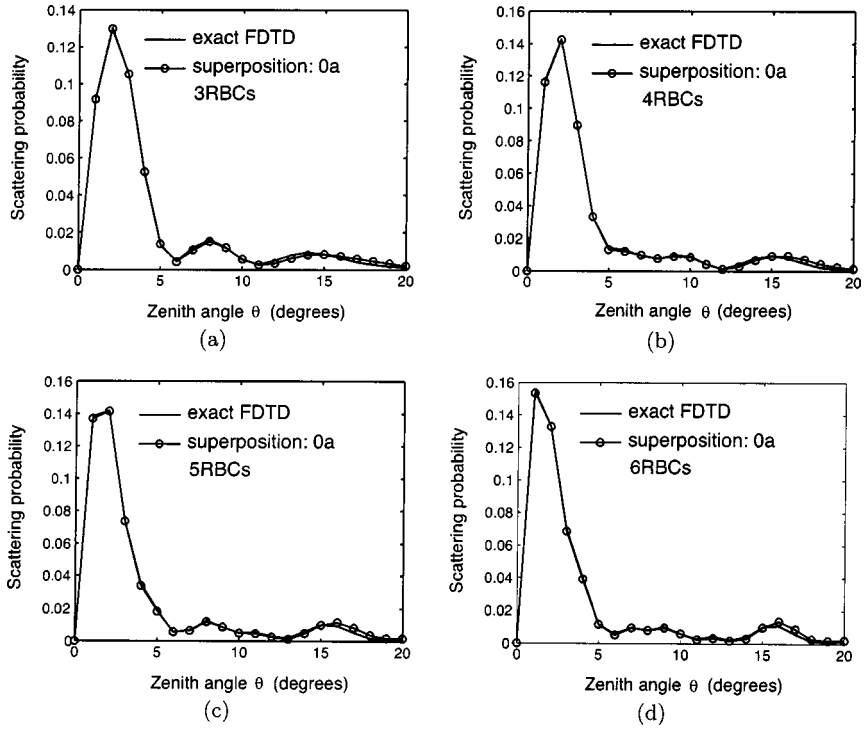

Fig. 13. Same case as that in Fig. 8 but with more than two RBCs (number of cells given in the labeling in each plot).

Table 1. Radiated Powers of RBCs with Different Background Refractive Indices

Radiated Power	n_r		
	1.045	1.020	1.010
P (FDTD)	1.39×10^{-13}	3.33×10^{-14}	8.72×10^{-15}
P [Eq. (13)]	1.60×10^{-13}	3.40×10^{-14}	8.76×10^{-15}

employed to study the multiple-scattering properties between RBCs. The calculations show that the lateral multiple scattering between RBCs is very weak. As a result, approximate methods are accurate. Meanwhile, the multiple scattering between RBCs located along the incident wave direction cannot be neglected. Hence superposition and the simplest form of the Rytov approximation do not give accurate results in that case. However, the results of the DDA method, which is a more accurate method, agree with the FDTD results.

For the applications in this paper, the DDA method is faster than the FDTD method and requires less memory. Hence it is a strong alternative to the FDTD method. The Rytov approximation is less accurate than the DDA and FDTD methods. However, it is a simple method that can easily be implemented on a computer. It provides accurate results for geometries similar to the one in Fig. 3(c).

ACKNOWLEDGMENT

We acknowledge the Swedish Research Council for its financial support of this project.

J. He is also at Zhejiang University, Zhejiang, China.

REFERENCES

1. T. Johansson, M. S. T. Thompson, M. Stenberg, C. af Klinteberg, S. Andersson-Engels, S. Svanberg, and K. Svanberg, "Feasibility study of a novel system for combined light dosimetry and interstitial photodynamic treatment of massive tumors," Appl. Opt. **41**, 1462–1468 (2002).
2. S. Iinuma, K. T. Schomacker, G. Wagnieres, M. Rajadhyaksha, M. Bamberg, T. Momma, and T. Hasan, "*In vivo* fluence rate and fractionation effects on tumor response and photobleaching: photodynamic therapy with two photosensitizers in an orthotopic rat tumor model," Cancer Res. **59**, 6164–6170 (1999).
3. L. Lilge, K. Molpus, T. Hasan, and B. C. Wilson, "Light dosimetry for intraperitoneal photodynamic therapy in a murine xenograft model of human epithelial ovarian carcinoma," Photochem. Photobiol. **68**, 281–288 (1998).
4. I. J. Bigio, S. G. Bown, G. Briggs, S. Lakhanic, D. Pickard, P. M. Ripley, I. G. Rose, and C. Saunders, "Diagnosis of breast cancer using elastic-scattering spectroscopy: preliminary clinical results," J. Biomed. Opt. **5**, 221–228 (2000).
5. I. J. Bigio, J. R. Mourant, and G. Los, "Noninvasive, *in-situ* measurement of drug concentrations in tissue using optical spectroscopy," J. Gravit. Physiol. **6**, 173–175 (1999).
6. J. R. Mourant, T. M. Johnson, G. Los, and I. J. Bigio, "Noninvasive measurement of chemotherapy drug concentrations in tissue: preliminary demonstrations of *in vivo* measurements," Phys. Med. Biol. **44**, 1397–1417 (1999).
7. G. Mazarevica, T. Freivalds, and A. Jurka, "Properties of erythrocyte light refraction in diabetic patients," J. Biomed. Opt. **7**, 244–247 (2002).
8. Y. L. Kim, Yang Liu, R. K. Wali, H. K. Roy, M. J. Goldberg, A. K. Kromin, Kun Chen, and V. Backman, "Simultaneous measurement of angular and spectral properties of light scattering for characterization of tissue microarchitecture and its alteration in early precancer," IEEE J. Sel. Top. Quantum Electron. **9**, 243–256 (2003).
9. J. He, A. Karlsson, J. Swartling, and S. Andersson-Engels, "Numerical simulations of light scattering by red blood cells," Tech. Rep. LUTEDX/(TEAT-7116) (Lund Institute of Technology, Department of Electroscience, P.O. Box 118, S-221 00 Lund, Sweden, 2003).

10. L. Wang, S. L. Jacques, and L. Zheng, "MCML—Monte Carlo modeling of light transport in multi-layered tissues," Comput. Methods Programs Biomed. **47**, 131–146 (1995).
11. S. V. Tsinopoulos, E. J. Sellountos, and D. Polyzos, "Light scattering by aggregated red blood cells," Appl. Opt. **41**, 1408–1417 (2002).
12. E. Evans and Y. Fung, "Improved measurement of the erythrocyte geometry," Microvasc. Res. **4**, 335–347 (1972).
13. P. Alsholm, "Light scattering by individual and groups of spheroidal particles," Tech. Rep. LRAP-200, Lund reports on Atomic Physics (Lund Institute of Technology, Lund, Sweden, 1996).
14. R. A. Meyer, "Light scattering from red blood cell ghosts: sensitivity of angular dependent structure to membrane thickness and refractive index," Appl. Opt. **16**, 2036–2037 (1977).
15. J. C. Lin and A. W. Guy, "A note on the optical scattering characteristics of whole blood," IEEE Trans. Biomed. Eng. **21**, 43–45 (1974).
16. R. Drezek, A. Dunn, and R. Richards-Kortum, "Light scattering from cells: finite-difference time-domain simulations and goniometric measurements," Appl. Opt. **38**, 3651–3661 (1999).
17. R. Drezek, M. Guillaud, T. Collier, A. Malpica, C. Macaulay, M. Follen, and R. Richards-Kortum, "Light scattering from cervical cells throughout neoplastic progression: influence of nuclear morphology, DNA content, and chromatin texture," J. Biomed. Opt. **8**, 7–16 (2003).
18. R. Drezek, A. Dunn, and R. Richards-Kortum, "A pulsed finite-difference time-domain (FDTD) method for calculating light scattering from biological cells over broad wavelength ranges," Opt. Express **6**, 147–157 (2000).
19. A. Dunn, C. Smithpeter, A. Welch, and R. Richards-Kortum, "Finite-difference time-domain simulation of light scattering from single cells," J. Biomed. Opt. **2**, 262–266 (1997).
20. D. Arifler, M. Guillaud, A. Carraro, A. Malpica, M. Follen, and R. Richards-Kortum, "Light scattering from normal and dysplastic cervical cells at different epithelial depths: finite-difference time-domain modeling with a perfectly matched layer boundary condition," J. Biomed. Opt. **8**, 484–494 (2003).
21. A. Taflove, *Computational Electrodynamics: The Finite-Difference Time-Domain Method* (Artech House, Boston, 1995).
22. J. P. Berenger, "A perfectly matched layer for the absorption of electromagnetic waves," J. Comput. Phys. **114**, 185–200 (1994).
23. B. T. Draine and P. J. Flatau, "Discrete-dipole approximation for scattering calculations," J. Opt. Soc. Am. A **11**, 1491–1499 (1994).
24. A. Ishimaru, *Electromagnetic Wave Propagation, Radiation, and Scattering* (Prentice Hall, Englewood Cliffs, N.J., 1991).
25. B. T. Draine, *Light Scattering by Nonspherical Particles: Theory, Measurements, and Applications* (Academic, New York, 2000).
26. V. I. Tatarski, *Wave Propagation in a Turbulent Medium* (McGraw-Hill, New York, 1961).
27. A. C. Kak and M. Slaney, *Principles of Computerized Tomographic Imaging* (IEEE Press, Piscataway, N.J., 1988).
28. http://www.semcad.com/.
29. A. M. K. Enejder, "Light scattering and absorption in tissue—models and measurements," Ph.D. thesis (Lund Institute of Technology, Lund, Sweden, 1997).
30. A. M. K. Nilsson, P. Alsholm, A. Karlsson, and S. Andersson-Engels, "*T*-matrix computations of light scattering by red blood cells," Appl. Opt. **37**, 2735–2748 (1998).
31. L. Tsang, J. A. Kong, and K.-H. Ding, *Scattering of Electromagnetic Waves: Theories and Applications* (Wiley, New York, 2000).
32. S. V. Tsinopoulos and D. Polyzos, "Scattering of He–Ne laser light by an average-sized red blood cell," Appl. Opt. **38**, 5499–5510 (1999).